ISIJ International, Vol. 53 (2013), No. 5, pp. 774–781

Effect of Oxygen Partial Pressure on the Formation Mechanisms of Complex Ca-rich Ferrites

Nathan A. S. WEBSTER,[1,2)]* Mark I. POWNCEBY,[1)] Ian C. MADSEN[1)] and Justin A. KIMPTON[3)]

1) CSIRO Process Science and Engineering, Box 312, Clayton South, VIC, 3169 Australia.
2) Australian Nuclear Science and Technology Organisation, Locked Bag 2001, Kirrawee DC, NSW, 2232 Australia.
3) Australian Synchrotron, 800 Blackburn Rd, Clayton, VIC, 3168 Australia.

(*Received on December 19, 2012; accepted on February 19, 2013*)

The formation mechanisms of the complex Ca-rich ferrite iron ore sinter bonding phases SFCA and SFCA-I, during heating of a synthetic sinter mixture in the range 298–1 623 K and at pO_2 = 0.21, 5×10^{-3} and 1×10^{-4} atm, were determined using *in situ* X-ray diffraction. SFCA and, in particular, SFCA-I are desirable bonding phases in iron ore sinter, and improved understanding of the effect of parameters such as pO_2 on their formation may lead to improved ability to maximise their formation in industrial sintering processes. SFCA-I and SFCA were both observed to form at pO_2 = 0.21 and 5×10^{-3} atm, with the formation of SFCA-I preceding SFCA formation in each case, but via distinctly different mechanisms at each pO_2. No SFCA-I was observed at $pO_2 = 1 \times 10^{-4}$ atm; instead, a Ca-rich phase designated CF_{AlSi}, formed at 1 420 K. By 1 456 K, CF_{AlSi} had decomposed to form melt and a small amount of SFCA. Such a low pO_2 during heating of industrial sinter mixtures is, therefore, undesirable, since it would not result in the formation of an abundance of SFCA and SFCA-I bonding phases. In addition, CFA phase, which was determined by Webster *et al*. (*Metall. Mater. Trans. B*, 43(2012), 1344) to be a key precursor phase in the formation of SFCA at $pO_2 = 5 \times 10^{-3}$ atm, was also observed to form at pO_2 = 0.21 and 1×10^{-4} atm, with the amount decreasing with increasing pO_2.

KEY WORDS: iron ore sinter; complex Ca-rich ferrite sinter bonding phases; SFCA and SFCA-I; *in situ* X-ray diffraction; oxygen partial pressure; phase formation mechanisms; synchrotron X-ray diffraction.

1. Introduction

Iron ore < 6.3 mm in size is too fine for direct use in a blast furnace and must first be agglomerated into iron ore sinter. Sinter is often the major component of blast furnace burden, and the production of high quality sinter is important for efficient blast furnace operation. During the iron ore sintering process, these iron ore fines are mixed with fluxes (*e.g*. limestone) and coke breeze and rapidly heated in 2–4 min to temperatures of ~1 573 K, followed by slower cooling in air.[1)] This results in partial melting of the mixture and converts the loose raw materials into a porous but physically strong composite material in which the iron-bearing minerals (40–70 vol% hematite, Fe_2O_3, and magnetite, Fe_3O_4) are bonded together by a matrix containing complex Ca-rich ferrite phases (20–50 vol%), glasses (quenched melt) and calcium silicates (each up to 10 vol%).[2)] Oxygen partial pressure (pO_2) values range from reducing during the initial stages of sintering as the coke breeze is consumed to oxidising during cooling.[3,4)]

The complex Ca-rich ferrite bonding phases typically also contain some silica and alumina and are known collectively by the acronym 'SFCA', which stands for Silico-Ferrite of Calcium and Aluminium.[5)] Other ferrite phases observed in industrial sinters include monocalcium ferrite, $CaO.Fe_2O_3$ (abbreviated to CF), dicalcium ferrite, $2CaO.Fe_2O_3$ (C_2F), hemicalcium ferrite, $CaO.2Fe_2O_3$ (CF_2) and brownmillerite ($2CaO.(Al_2O_3).(Fe_2O_3)$, C_2AF, *i.e*. A = Al_2O_3).[6)] SFCA phases are believed to be the most desirable bonding phases in iron ore sinter because of their high reducibility,[7)] high mechanical strength and low reduction degradation,[8,9)] all of which are significant factors in determining the productivity and efficiency of the blast furnace.

The SFCA produced in iron ore sinter has, in the past, been divided on the basis of composition, structure and morphology into two main types. One is a high-Fe, low-Si form called SFCA-I, which has been described as having a platy morphology but also as being acicular. Mumme *et al*.[10)] reported that an SFCA-I found in plant sinter contained 84 mass% Fe_2O_3, 13 mass% CaO, 1 mass% SiO_2 and 2 mass% Al_2O_3, and also synthesised material with the SFCA-I structure which had composition 83.15 mass% Fe_2O_3, 12.61 mass% CaO and 4.24 mass% Al_2O_3. The second 'SFCA' type is a low-Fe form that is simply referred to as SFCA and which exhibits a prismatic or columnar morphology in polished sections. SFCA found in industrial, plant sinters typically contains 60–76 mass% Fe_2O_3, 13–16 mass% CaO, 3–10 mass% SiO_2, 4–10 mass% Al_2O_3 and 0.7–1.5 mass% MgO.[11,12)] Patrick and Pownceby[13)] systematically resolved

* Corresponding author: E-mail: nathan.webster@csiro.au
DOI: http://dx.doi.org/10.2355/isijinternational.53.774

the equilibrium solid solution range and thermal stability of SFCA within the quaternary system Fe_2O_3–CaO–SiO_2–Al_2O_3 in air at 1 513–1 663 K. More recently a third SFCA with composition 67.3 mass% Fe_2O_3, 12.3 mass% CaO and 20.4 mass% Al_2O_3 and designated SFCA-II was reported by Mumme.[14] It has been reported to be present in plant sinters from South Africa.[15,16]

McAndrew and Clout[17] suggested that the texture of intersecting microplates of SFCA-I imparts superior strength and easier reducibility, and sinters containing significant amounts of this phase are of high quality. By comparison, sinters containing high amounts of prismatic SFCA, which is usually associated with glass, are typically weaker, have lower reducibility and are generally of lower quality. The effect of SFCA-II on strength and reducibility of iron ore sinter is unknown.

A large number of investigations[2,3,18–25] have aimed to determine the formation mechanisms of complex Ca-rich ferrite phases. Increased understanding of the mechanisms has the potential to improve the efficiency of the sintering process by a) being able to predict the optimal sintering conditions (temperature, pO_2) to produce high quality product based on the chemical and physical composition of the iron ore fines, and b) being able predict the chemical and physical modifications of a particular iron ore fines mixture required to produce high quality product. Both are becoming increasingly important as the total iron content in many iron ores is decreasing and the concentration of alumina and silica-containing gangue minerals is increasing.

In the most recent of these mechanistic investigations, Webster *et al*.[25] implemented *in situ* X-ray diffraction (XRD) in order to determine the SFCA and SFCA-I formation mechanisms in synthetic iron ore sinter mixtures, containing 1, 5 and 10 mass% Al_2O_3, in the range 298–1 623 K and at an oxygen partial pressure of 5×10^{-3} atm. The selection of the pO_2 was based on work of Hsieh and Whiteman,[2] where it was shown that this oxygen partial pressure maximised the formation of Ca-rich ferrite phases, whilst producing mineral assemblages similar to those found in industrial sinters. Webster *et al*.[25] showed that during heating, SFCA-I formation was associated with reaction between Fe_2O_3, SiO_2 and Al_2O_3-substituted C_2F [*i.e*. $C_2(F_{1-x}A_x)$]. In contrast, SFCA formation was associated with reaction between CF, SiO_2 and a phase designated CFA which had average composition 71.7 mass% Fe_2O_3, 12.9 mass% CaO, 0.3 mass% SiO_2 and 15.1 mass% Al_2O_3. The initial formation of SFCA at ~1 433 K was independent of SFCA-I, however at higher temperature (T > 1 473 K) SFCA-I was consumed in the formation of SFCA. Eqs. (1) and (2) (unbalanced) summarise the reactions involved in the formation of SFCA-I and SFCA determined by Webster *et al*.[25] (the '±' in Eq. (2) represents the initial formation of SFCA being independent of SFCA-I).

$$Fe_2O_3 + C_2(F_{1-x}A_x) + SiO_2 \rightarrow \text{SFCA-I} \quad \text{..... (1)}$$

$$CF + CFA + Fe_2O_3 + SiO_2 + \text{Al-oxide} \pm \text{SFCA-I} \rightarrow \text{SFCA} \quad \text{..... (2)}$$

Increasing Al_2O_3 concentration in the starting sinter mixture increased the temperature range over which SFCA-I was stable before the initial formation of SFCA. Increasing Al_2O_3 concentration also increased the stability range of SFCA before it melted to form a Fe_3O_4 + melt phase assemblage.

The formation of CFA during heating had not been described in a previous *in situ* XRD investigation of reaction sequences in the formation of SFCA phases, which was performed under vacuum in the range 298–1 533 K by Scarlett *et al*.[23,24] Eqs. (3) and (4) summarise the reactions involved in the formation of SFCA-I and SFCA determined by Scarlett *et al*.:

$$Fe_2O_3 + CF + SiO_2 + \text{Al-oxide} \rightarrow \text{SFCA-I} \quad \text{..... (3)}$$

$$Fe_2O_3 + CF + SiO_2 + \text{Al-oxide} \pm \text{SFCA-I} \rightarrow \text{SFCA} \quad \text{..... (4)}$$

Based on the absence of Fe_3O_4 in the study of Scarlett *et al*.[23,24] it was inferred by Webster *et al*.[25] that the oxygen partial pressure was somewhere in the range $0.21 - 5 \times 10^{-3}$ atm, and it was speculated that pO_2 may affect the formation of CFA. Given that CFA was a precursor phase involved in the formation of the SFCA phases in the study of Webster *et al*.,[25] it is also likely that pO_2 would exert an influence on the formation mechanisms of SFCA and SFCA-I during heating. The purpose of the current investigation was to determine the effect of pO_2 on the formation of CFA, and also on the formation of SFCA and SFCA-I bonding phases, during the heating of a synthetic sinter starting mixture. A series of *in situ* XRD and phase equilibria experiments were performed over the range 298–1 623 K and at pO_2 values of 0.21, 5×10^{-3} and 1×10^{-4} atm in order to characterise the phase evolution.

2. Experimental

2.1. Starting Sinter Mixture Preparation

The nominal concentration of the synthetic starting sinter mixture for the *in situ* XRD experiments, in terms of mass% of oxides, was 77.36, 14.08, 3.56 and 5.00 mass% Fe_2O_3, CaO, SiO_2 and Al_2O_3, respectively. This mixture was equivalent to mixture SM4/5 previously investigated by Webster *et al*.[25] and was designed to maximise the formation of the SFCA phase.[13] It was prepared from fine grained (< 20 μm) synthetic Fe_2O_3 (Acros Organics, 99.999%), calcite, $CaCO_3$ (Thermo Fisher, 99.95%), quartz, SiO_2 (Sigma Aldrich, 99.995), and gibbsite, $Al(OH)_3$ (Alcan OP25 Super White, 99.9%); these were mixed under acetone in a mortar and pestle. In terms of its relevance to a typical industrial iron ore sinter mixture of fines, flux and coke, this composition is indicative of the reactive ultra-fine coating component of the mixture (< ~1 mm), rather than the bulk composition which also includes larger 'nuclei' ore particles.

2.2. *In Situ* XRD

In situ XRD experiments were performed using an INEL diffractometer, which incorporates a CPS120 position-sensitive detector allowing for simultaneous collection of up to 120° 2θ of diffraction data. The Co tube was operated at 40 kV and 35 mA. An Anton Paar model HTK 10 high temperature chamber, employing a platinum resistance strip heater inside it, was positioned on the instrument (**Fig. 1**). A slurry of the sinter sample mixture and ethanol was prepared and placed into a sample well, measuring approximately 20 × 7 × 0.2 mm, on the platinum heater.

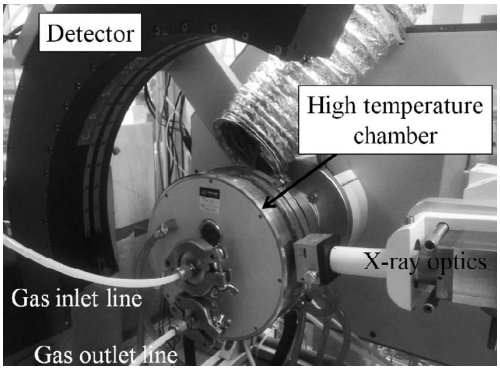

Fig. 1. The high temperature chamber fitted to the laboratory INEL X-ray diffractometer.

The experimental pO_2 values of 0.21, 5×10^{-3} and 1×10^{-4} atm were obtained by flowing compressed air, and special gas mixtures containing 0.5 and 0.01% O_2 in N_2 (BOC Gases), respectively, into the Anton Paar chamber. Before each experiment the chamber was purged for 10 min by a flow (~ 1 L min^{-1}) of the designated gas mixture, after which the sample was heated under a continuous flow of the gas.

A heating rate of 20 K min^{-1} was used from 298 to 873 K (approaching the decomposition temperature of $CaCO_3$), then a slower rate of 10 K min^{-1} to 1 623 K was used during the period of SFCA-I and SFCA phase formation and melting. The temperature was measured by a Pt/PtRh10% thermocouple connected to the underside of the platinum strip. *In situ* XRD data were collected throughout heating, with individual datasets collected for 0.5 min. Data were collected in asymmetrical diffraction geometry with an incident beam angle of 10º, over the range $10º \leq 2\theta \leq 112º$. The temperatures of phase formation/transformation given throughout the manuscript are those at the start, which is when the temperatures were automatically recorded, of the relevant dataset. The uncertainty in these temperature values, therefore, was the difference between the temperatures at the start of successive datasets, and the magnitude of the uncertainty depended on the heating rate (*i.e.* 10 and 5 K for the 20 and 10 K min^{-1} heating regimes, respectively).

For the purposes of visualisation of the decomposition and formation of phases as the experiment progressed, the datasets were stacked to produce a plot of accumulated data with temperature plotted *vs* 2θ, viewed down the intensity axis (**Figs. 2**(a), 2(b) and 2(c)). Rietveld refinement was performed using TOPAS,[26] with the crystal structure information provided in Blake *et al.*, Maslen *et al.*, Saalfeld and Wedde, Lager *et al.*, Oftedal, Bersetegui *et al.*, Decker and Kasper, and Hamilton used for Fe_2O_3, $CaCO_3$, $Al(OH)_3$, SiO_2, CaO, $C_2(F_{1-x}A_x)$, CF and Fe_3O_4, respectively.[27–34] Single peak fitting to extract reflection intensities was also performed using TOPAS, with reflections modelled using a pseudo-Voigt profile function. The background was modelled using a Chebychev polynomial function.

2.3. Heat/Quench Experiments and Microscopic Characterisation

Laboratory heat/quench experiments were performed in order to investigate key phases revealed by the *in situ* XRD experiments in more detail. For these experiments, 0.5 g of the starting sinter mixture was pelletised and heated in a platinum crucible in a vertical tube furnace under the required pO_2 condition, followed by water quenching. The temperature adjacent to the crucible was measured using a Pt/PtRh13% thermocouple connected to an ice-point cell, and the temperature is considered accurate to ± 10 K.

Scanning electron microscopy (SEM) was performed using a FEI Quanta 400 Field Emission Environmental SEM operated at an accelerating voltage of 10 kV and a working distance of 10 mm. Energy dispersive spectroscopy (EDS) was performed on this instrument using a Bruker X-Flash 5010 Si-drift EDS detector. Electron probe microanalysis (EPMA) was performed using a JEOL JXA-8900F Superprobe. Fe_2O_3, wollastonite ($CaSiO_3$, CS) and "Magalox" (a synthetic spinel, composition $MgAl_2O_4$) were used as standards for the microprobe analyses which were conducted in wavelength dispersive mode using an accelerating voltage of 10 kV, a beam diameter of $< 1\,\mu$m and counting times of 15 sec.

2.4. Synthesis and Characterisation of SFCA and SFCA-I Materials

Synthesis of SFCA and SFCA-I materials, in order to investigate their structures in more detail, was carried out by heating pellets of the desired mixtures in a vertical tube furnace in air at 1 533 K for 24 hr. This was followed by air quenching, grinding, re-pelletising, and reheating for a further 24 hr followed by air quenching. This process was repeated to produce the final materials with a total heating time of 72 hr. EPMA data were collected using the procedure in Section 2.3.

Synchrotron XRD (S-XRD) data were collected for these materials, at room temperature on the powder diffraction beamline at the Australian Synchrotron[35] over the range $2º \leq 2\theta \leq 82.5º$. Samples were contained within 0.3 mm glass capillaries which were continuously rotated during data collection to improve particle statistics and to reduce the effects of preferred orientation. The X-ray wavelength was 0.7279 Å, calibrated using LaB_6 (NIST 660b line position and profile standard) contained in a 0.3 mm ID capillary. Pawley refinements[36] of the S-XRD data were performed using TOPAS. The triclinic ($P\bar{1}$) unit cell information for SFCA (a = 9.050, b = 10.025, c = 10.927 Å, α = 60.46, β = 73.79, γ = 65.94°) and SFCA-I (a = 10.431, b = 10.610, c = 11.839 Å, α = 94.14, β = 111.35, γ = 110.27°) described by Mumme *et al.*[10] were used as the starting parameters for the refinements.

For determination of Fe^{2+} content, the materials were dissolved with hydrofluoric and hydrochloric acids. The resulting solutions were then titrated to the electrochemical equivalence point against a standard dichromate solution using a 798 Metrohm MPT Titrino autotitrator. The Fe^{2+} content was calculated from the titre volumes.

3. Results and Discussion

Figure 2(a) shows the plot of accumulated *in situ* XRD data for the $pO_2 = 5 \times 10^{-3}$ atm experiment. The results, in terms of the phases observed and the temperature range of their stability, are in excellent agreement with those reported previously by Webster *et al.*[25] for the corresponding experiment for this sinter mixture composition performed at the Australian Synchrotron and for which the reaction mecha-

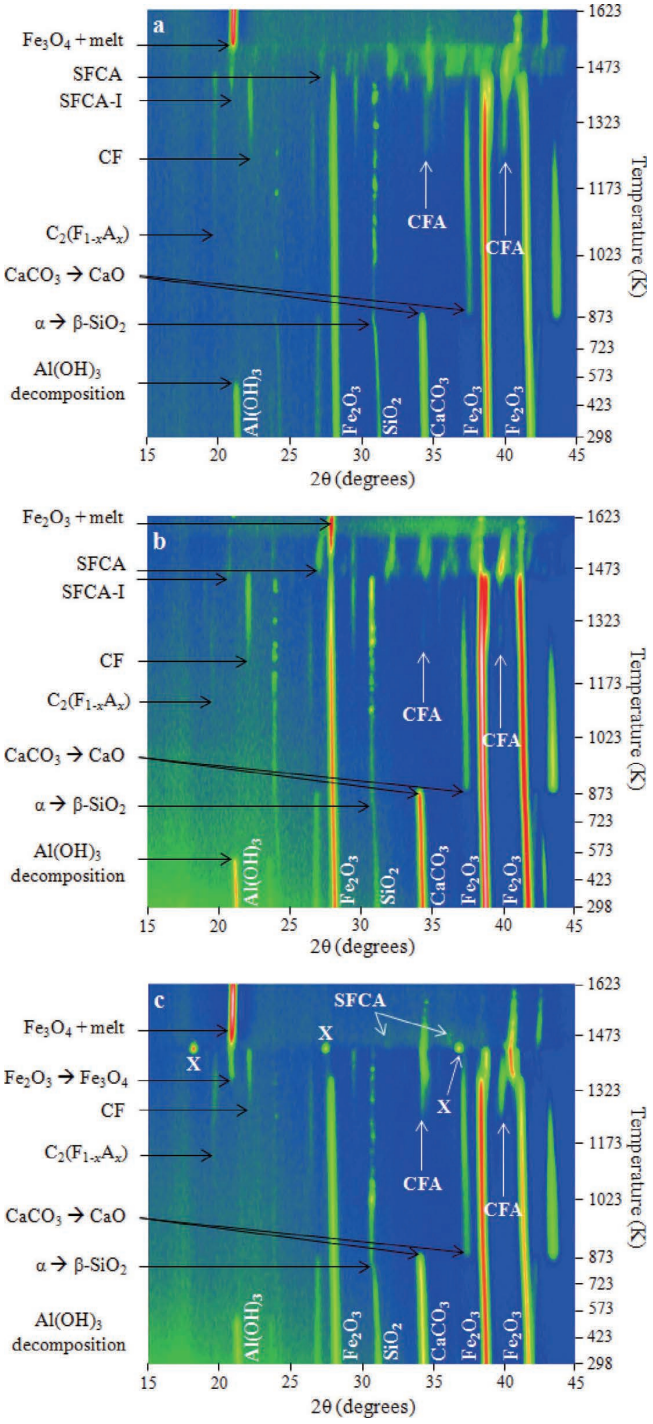

Fig. 2. *In situ* XRD data collected at a) $pO_2 = 5 \times 10^{-3}$ atm, b) 0.21 atm and c) 1×10^{-4} atm. Annotated on the plots are: the major reflections for materials in the starting mixture; the low-temperature (< 923 K) phase transformation ($\alpha \rightarrow \beta$-SiO_2) and decomposition (*e.g.* $CaCO_3 \rightarrow CaO$) events; the formation events of $C_2(F_{1-x}A_x)$, CF, SFCA-I, SFCA, the Fe_3O_4 + melt phase assemblage (for a and c), and the Fe_2O_3 + melt phase assemblage (for b); and the major reflections for CFA. X denotes the reflections for the unknown phase (for c).

nisms presented in Eqs. (1) and (2) applied. More specifically, $Al(OH)_3$ decomposition to an amorphous Al-oxide was complete by 562 K, transformation of the α-form of SiO_2 to β-SiO_2 was complete by 845 K (in excellent agreement with the 846 K reported by Kihara,[37] which gives a high level of confidence in the accuracy of the thermocouple), and decomposition of $CaCO_3$ to CaO was complete by 883 K. The first Ca-rich ferrite to form was $C_2(F_{1-x}A_x)$ at 1 037 K, followed by CF and CFA at 1 243 K, SFCA-I at 1 377 K, and SFCA at 1 441 K. Melting of both SFCA-I and SFCA was complete by 1 532 K, after which the Fe_3O_4 + melt phase assemblage had formed. Fe_3O_4 formed as a result of incongruent melting of SFCA, since Fe_2O_3 was fully consumed in the reactions to form the 'SFCA' phases by 1 472 K, which is before the predicted $Fe_2O_3 \rightarrow Fe_3O_4$ transformation temperature of 1 513 K.[38] **Table 1** summarises the formation temperatures of these phases and phase assemblages.

Table 1. Temperatures of formation of the significant phases and phase assemblages observed in the *in situ* XRD data collected at $pO_2 = 0.21$, 5×10^{-3} and 1×10^{-4} atm.

pO_2 (atm)	Temperature (K)					
	$C_2(F_{1-x}A_x)$	CF/CFA	SFCA-I	X (*i.e.* CF_{AlSi})	SFCA	Fe_3O_4 + melt/ Fe_2O_3 + melt
0.21	1 027	1 223	1 416	–	1 446	1 594
5×10^{-3}	1 037	1 243	1 377	–	1 441	1 532
1×10^{-4}	1 027	1 230	–	1 420	1 438	1 479

Figures 2(b) and 2(c) show the plots of accumulated *in situ* XRD data for the experiments conducted at $pO_2 = 0.21$ and 1×10^{-4} atm, respectively. The low temperature (< 923 K) phase decomposition and transformation events are very similar to those in Fig. 2(a). Oxygen partial pressure, therefore, does not have a significant effect on these events. In addition, pO_2 does not have a significant effect on the initial formation temperature of $C_2(F_{1-x}A_x)$ and CF (Table 1).

In contrast, however, pO_2 did have an effect on the stability of Fe_2O_3. At $pO_2 = 1 \times 10^{-4}$ atm, Fe_3O_4 formed through the $Fe_2O_3 \rightarrow Fe_3O_4$ reduction reaction which was complete by 1 367 K, in good agreement with the theoretical value of 1 371 K.[38] In the 0.21 atm experiment Fe_3O_4 did not form, with Fe_2O_3 remaining stable up to 1 623 K. In air the $Fe_2O_3 \rightarrow Fe_3O_4$ reduction reaction is predicted to occur within the range 1 623–1 682 K; the presence of labile Ca^{2+} in the system will likely displace the reaction to lower temperature than the theoretical value of 1 682 K.[38,39]

3.1. CFA Formation

Similarly to the experiment at $pO_2 = 5 \times 10^{-3}$ atm, characteristic CFA reflections were observed at $pO_2 = 0.21$ and 1×10^{-4} atm, occurring at 34.5 and 39.9° 2θ (d = 3.02 and 2.62 Å, respectively, annotated in Figs. 2(b) and 2(c)). The reflections in the experiment at $pO_2 = 0.21$ atm appeared to be of lower relative intensity to those in the other experiments, suggesting less CFA was formed under the more oxidising conditions. In the absence of previously published structural information for CFA necessary to perform Rietveld refinement-based quantitative phase analysis (QPA) of this phase, and also the absence of single-phase CFA material necessary to perform QPA using the PONKCS method,[40] an alternative method was required in order to confirm that the amount of CFA formed at $pO_2 = 0.21$ atm was less than at the other pO_2 values. In the alternative approach, the intensity (I_{CFA}) of the major CFA-phase reflection with d = 2.62 Å was normalised by the intensity of the major Fe_2O_3 reflection (I_{Hem}) at 38.8° 2θ in the dataset collected at room temperature. **Figure 3** shows I_{CFA}/I_{Hem} as a function of temper-

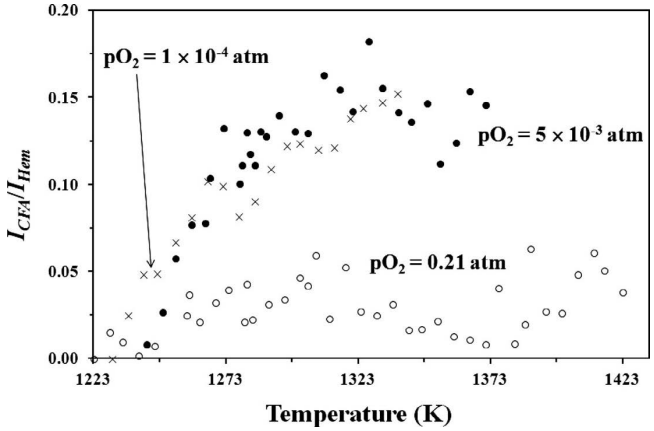

Fig. 3. The variation in normalised intensity, I_{CFA}/I_{Hem}, of the characteristic CFA reflection (d = 2.62 Å) as a function of temperature and pO_2.

ature for each pO_2.

For the experiment at $pO_2 = 5 \times 10^{-3}$ atm I_{CFA}/I_{Hem} is plotted from 1 223 to 1 371 K (*i.e.* just before the initial formation temperature of SFCA-I) due to significant overlap between the CFA and SFCA-I reflections. For the same reason I_{CFA}/I_{Hem} is plotted up to 1 412 K for the $pO_2 = 0.21$ atm experiment, while for the $pO_2 = 1 \times 10^{-4}$ atm experiment it is plotted to 1 338 K (*i.e.* just before the initial formation temperature of Fe_3O_4), due to overlap between the CFA and Fe_3O_4 reflections. Figure 3 confirms that the amount of CFA that formed at $pO_2 = 0.21$ atm was less than at the more reduced pO_2 values, and that the amount of CFA formed at $pO_2 = 5 \times 10^{-3}$ and $pO_2 = 1 \times 10^{-4}$ atm was similar.

3.2. SFCA and SFCA-I Phase Formation and Melting

Similar to the experiment at $pO_2 = 5 \times 10^{-3}$ atm, SFCA-I and SFCA were observed to form at $pO_2 = 0.21$ atm, at 1 416 and 1 446 K, respectively. Melting of both SFCA phases was complete by 1 594 K, producing the Fe_2O_3 + melt phase assemblage. For the $pO_2 = 1 \times 10^{-4}$ atm experiment, very weak reflections for SFCA were observed; SFCA initially formed at 1 438 K and was present until melting was complete by 1 479 K producing the Fe_3O_4 + melt phase assemblage. The decrease in melting point with decreasing pO_2 is in agreement with previous work.[39] Characteristic reflections for SFCA-I were not observed for the $pO_2 = 1 \times 10^{-4}$ atm experiment. Instead, reflections from an unknown phase (annotated with 'X' in Fig. 2(c)) were first observed at 1 420 K and were present until decomposition of this phase was complete at 1 456 K. No suitable match could be made between this phase and any phase within the Database of the International Centre for Diffraction Data (ICDD). However, based on the d-spacings of its reflections in Fig. 2(c) (5.66, 3.77 and 2.83 Å at 1 431 K), it appears likely to have a simple cubic crystal structure. Further work is required to determine the details of its crystal structure.

Based on a comparison of the three experiments the effect of decreasing pO_2 was to significantly decrease the thermal stability range of SFCA which was 1 446–1 594, 1 441–1 532 and 1 438–1 479 K at $pO_2 = 0.21$, 5×10^{-3} and 1×10^{-4} atm, respectively (see Table 1). In contrast, the effect of decreasing oxygen partial pressure from 0.21 to 5×10^{-3} atm was to stabilise the formation of SFCA-I at a lower temperature, and it is hypothesised that SFCA-I may accommodate more Fe^{2+} into its structure than SFCA.

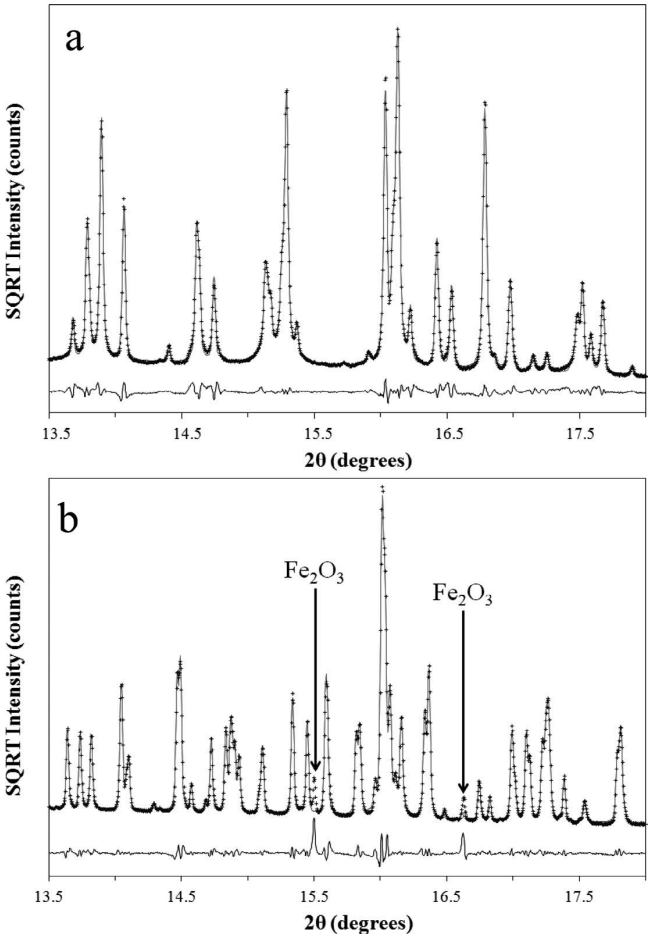

Fig. 4. Output of Pawley refinements to S-XRD data collected for a) SFCA; and b) SFCA-I synthesised at $pO_2 = 0.21$ atm at 1 533 K for 72 hr. The data are shown only at low 2θ values over a narrow angular range of the complete datasets. Experimental data are shown as plus signs, the calculated patterns are solid lines, and the difference patterns are the solid lines below. Fe_2O_3 reflections are annotated on the SFCA-I plot.

Table 2. Summary of the EPMA compositional results, in terms of mass% oxides, for the SFCA and SFCA-I materials synthesised at $pO_2 = 0.21$ atm at 1 533 K for 72 hr. The numbers in parentheses are the standard deviations of ~30 point analyses for each phase.

Sample	Composition (mass%)				
	Fe_2O_3	CaO	SiO_2	Al_2O_3	Total
SFCA	80.0 (1.2)	13.5 (0.3)	3.0 (0.2)	4.7 (0.1)	101.2 (1.2)
SFCA-I	83.5 (2.0)	12.9 (0.1)	0.0 (0.1)	5.0 (0.8)	101.5 (1.7)

Following on from the latter observation it is noted that in SFCA and SFCA-I materials synthesised in air in the range 1 473–1 573 K by Mumme *et al.*,[10] the SFCA-I contained a higher amount of Fe^{2+} in its structure compared with SFCA. However, the assignment of the amount of Fe^{2+} was based purely on charge balance considerations, and a more rigorous analytical approach was required to determine whether this is indeed the case. Here, SFCA and SFCA-I materials were synthesised in air at 1 533 K. **Table 2** shows the EPMA-determined compositions for each. **Figure 4** shows the output of

Pawley refinements to the high resolution S-XRD data collected for SFCA (Fig. 4(a)) and SFCA-I (Fig. 4(b)). The quality of the fit shown in Fig. 4(a) indicated that the SFCA was single phase; conversely the fit to the data collected for SFCA-I indicated the presence of a minor impurity phase, which was subsequently identified as Fe_2O_3 (ICDD No. 33-0664).

Subsequent Fe^{2+} determination via titration showed that the bulk SFCA and SFCA-I materials contained 0.46(0.01) and 1.38(0.01) mass% Fe^{2+}, respectively. If it is assumed that Fe_2O_3 contains Fe^{3+} only, then these results are in agreement with the hypothesis that SFCA-I can accommodate more Fe^{2+} than SFCA. Future work will aim to further test this hypothesis, by investigating the effect of oxygen partial pressure in the range $pO_2 = 0.21 - 1 \times 10^{-4}$ atm, on the equilibrium phase assemblages produced from these SFCA and SFCA-I starting mixtures at a number of temperatures in the range 1 423–1 573 K.

3.3. Characterisation of the Unknown Phase, $pO_2 = 1 \times 10^{-4}$ atm

The 'X' phase appears to be a short-lived transient phase, and attempts to quench-in this phase by heating pellets of the starting sinter mixture in a platinum crucible in a vertical tube furnace were unsuccessful. In order to quench-in X phase for *ex situ* examination using SEM, EDS and EPMA, a repeat *in situ* XRD experiment was performed, under the same conditions except that the sample was cooled at 200 K min^{-1} to 298 K once the temperature had reached 1 433 K (the temperature at which X phase reflections were most intense). Diffraction data were also collected during cooling, and the reflections for X phase, as well as Fe_3O_4 and SFCA, persisted down to 298 K. The product was then removed from the Pt strip heater and prepared for microscopic and compositional examination.

Figure 5 shows backscattered electron micrographs of the product of this experiment; Fig. 5(a) shows a grain containing Fe_3O_4 and X phase, and Fig. 5(b) shows a grain containing X phase and a dark-contrast phase which EDS suggested was likely to be quenched melt. **Table 3** shows the composition of each of these phases, determined using EMPA, assuming all Fe was present as Fe^{3+}. The results show that the Fe and Ca totals for X phase are similar to that for CF (*i.e.* 74 and 26 mass% Fe_2O_3 and CaO, respectively), and too Ca-rich and Fe-poor to be closely related to SFCA-I (see Section 1). X phase is renamed CF_{AlSi} throughout the remainder of the manuscript, which reflects its compositional similarity with CF and its low Al and Si content.

3.4. Reaction Mechanisms, $pO_2 = 1 \times 10^{-4}$ atm

Figure 6 shows the *in situ* XRD data collected over the range 1 401–1 456 K at $pO_2 = 1 \times 10^{-4}$ atm. The appearance and subsequent increase in intensity of the reflections for CF_{AlSi} at 1 420–1 431 K coincided with a decrease in intensity (and ultimately the disappearance) of the $C_2(F_{1-x}A_x)$, CF and SiO_2 reflections. Figures 6 and 2(c) showed that melting of CF_{AlSi} at temperatures above 1 438 K coincided with the appearance of the minor SFCA reflections, and an increase in the background which is consistent with the formation of melt.

Whilst not evident in Fig. 6, the formation of CF_{AlSi} did correspond with the consumption of some Fe_3O_4 and it is considered likely, therefore, that CF_{AlSi} contains a significant amount of Fe^{2+}. **Figure 7** shows the results of Rietveld-refinement based QPA, in the temperature range 1 073–1 456 K, performed for the $pO_2 = 1 \times 10^{-4}$ atm experiment. The values for phase concentration are absolute, rather than

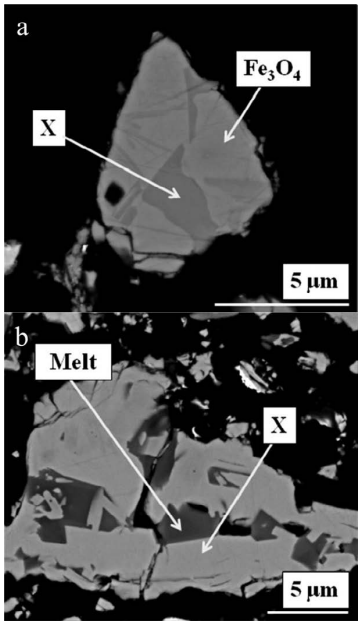

Fig. 5. Backscattered electron micrographs of the product of the *in situ* XRD experiment designed to quench in the unknown X phase. a) Shows regions of Fe_3O_4 and X phase, and b) shows regions of X phase and melt. The black areas are pores.

Table 3. Summary of the compositional results, in terms of mass% oxides, for the product of the *in situ* XRD experiment performed at $pO_2 = 1 \times 10^{-4}$ atm, where the sample was cooled from 1 433 K during heating at 200 K min^{-1} to 298 K. The numbers in parentheses are the standard deviations of triplicate point analyses for each phase.

Phase	Composition (mass%)				
	Fe_2O_3	CaO	SiO_2	Al_2O_3	Total
Fe_3O_4	96.5 (2.2)	2.5 (1.3)	0.1 (0.1)	1.5 (0.1)	100.5 (1.0)
X (*i.e.* CF_{AlSi})	71.6 (1.0)	24.1 (0.3)	0.3 (0.1)	2.4 (0.3)	98.5 (0.9)
Melt	19.2 (1.6)	37.4 (0.4)	18.9 (0.4)	21.6 (1.7)	97.1 (0.9)

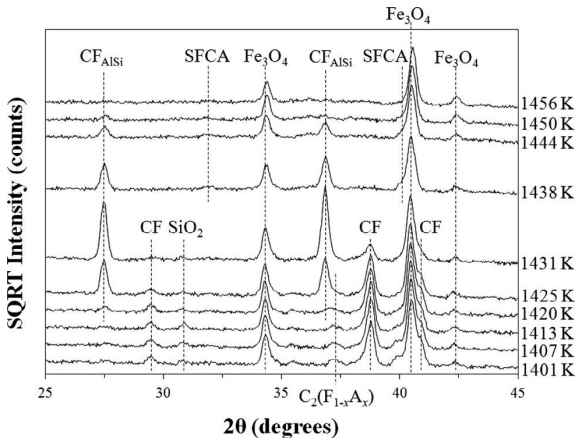

Fig. 6. *In situ* XRD data collected at $pO_2 = 1 \times 10^{-4}$ atm over the range 1 401–1 456 K. The datasets have been offset in the intensity axis to avoid overlap and improve clarity.

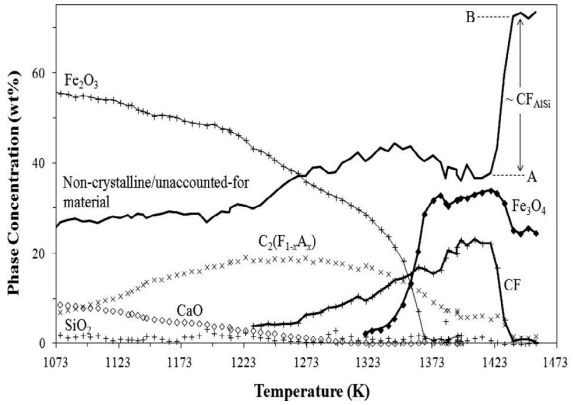

Fig. 7. Results of the Rietveld refinement-based quantitative phase analysis for the *in situ* XRD experiment performed at $pO_2 = 1 \times 10^{-4}$ atm. Shown are the absolute concentrations of the phases in the system as a function of temperature, which were calculated using the relationships shown in Eqs. (5) and (9).

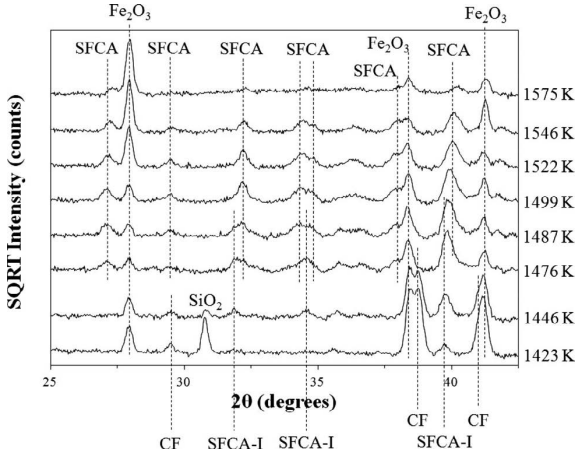

Fig. 8. *In situ* XRD data collected at $pO_2 = 0.21$ atm over the range 1 423–1 575 K. The datasets have been offset in the intensity axis to avoid overlap and improve clarity.

relative, values which were determined using the relationship shown in Eq. (5) (after Madsen and Scarlett[41]),

$$W_i = \frac{\mu_m^* S_i (ZMV)_i}{K} \quad \text{..... (5)}$$

Here, W_i is the weight fraction of phase i, S_i is the Rietveld scale factor of phase i, ZM is the unit-cell mass of the phase, V the unit-cell volume, μ_m^* is the mass absorption coefficient of the entire mixture, and K is a scaling factor used to put W_i on an absolute basis. K is constant during an experiment as long as the experimental conditions (*e.g.* mA and kV of the Co tube) do not change,[24,42,43] and was calculated using i) the known concentrations of Fe_2O_3, $CaCO_3$, SiO_2 and $Al(OH)_3$ in the starting mixture, and ii) the Rietveld-refined scale factors for Fe_2O_3, $CaCO_3$, SiO_2 and $Al(OH)_3$ in the first dataset collected at 25°C, using Eq. (6).

$$K = \frac{\mu_m^* \sum_{i=1}^{n} S_i (ZMV)_i}{\sum_{i=1}^{n} W_i} \quad \text{..... (6)}$$

In Fig. 7, a decrease in the Fe_3O_4 concentration at ~1 423 K corresponds with the formation of CF_{AlSi}, and the following plateau in concentration corresponds with the end of this reaction. Eqs. (7) and (8) summarise the reactions involved in the formation of CF_{AlSi} and SFCA at $pO_2 = 1 \times 10^{-4}$ atm:

$$C_2(F_{1-x}A_x) + CF + SiO_2 + Fe_3O_4 \rightarrow CF_{AlSi} \text{.....} (7)$$

$$CF_{AlSi} \rightarrow SFCA + melt \text{.....} (8)$$

The determination of absolute, rather than relative, concentrations in the manner described has the advantage of allowing for estimation of the non-crystalline/unaccounted-for phase content as a function of temperature. This was achieved using Eq. (9),[41] and the variation of the non-crystalline/unaccounted-for phase content, which includes CF_{AlSi} because its crystal structure details are unknown, is also shown in Fig. 7. Using this method the maximum possible concentration of CF_{AlSi} in the system is estimated as being ~35 mass% (*i.e.* the difference between levels B and A labelled in Fig. 7).

$$W_{unknown} = 100 - \sum_{i=1}^{n} W_i \quad \text{..... (9)}$$

3.5. Reaction Mechanisms, $pO_2 = 0.21$ atm

One of the key differences between the results of this experiment, and the results at $pO_2 = 5 \times 10^{-3}$ atm described by Webster *et al.*[25] and here in Eqs. (1) and (2), is that $C_2(F_{1-x}A_x)$, instead of being directly involved in the reaction to form SFCA-I, was fully consumed in its reaction with Fe_2O_3 to form CF and CFA *before* the formation of SFCA-I. **Figure 8** shows the *in situ* XRD data collected over the range 1 423–1 575 K at $pO_2 = 0.21$ atm. The typical $C_2(F_{1-x}A_x)$ reflections at 26.4 and 37.2° 2θ (d = 3.92 and 2.80 Å, respectively) are not present at 1 423 K which is before SFCA-I was first evident. A second difference from the results at $pO_2 = 5 \times 10^{-3}$ atm is that instead of the amount of CF increasing during the early stages of SFCA-I formation, CF was directly involved in the formation of SFCA-I, with the intensities of the CF reflections in Fig. 8 decreasing with the appearance, and subsequent increase in intensity, of the SFCA-I reflections. Both of these results correlate with those obtained by Scarlett *et al.*,[23,24] which is evidence that their experiments which yielded the SFCA-I and SFCA formation mechanisms shown in Eqs. (3) and (4) were conducted towards the high pO_2 end of the range $pO_2 = 0.21 - 5 \times 10^{-3}$ atm. The formation of SFCA-I was also associated with a decrease in intensity of the Fe_2O_3 and SiO_2 reflections. Further formation of SFCA-I, and the initial formation of SFCA, resulted in a further decrease in intensity of the Fe_2O_3 reflections and the disappearance of the SiO_2 reflections.

Given the low intensity of the CFA reflections, and the overlap of the major CFA reflection at 39.9° 2θ with a major SFCA-I reflection, it is difficult to determine from these *in situ* data whether, like CF, CFA was involved in the reaction to form SFCA-I or, as was the case at $pO_2 = 5 \times 10^{-3}$ atm, it was only involved in the reaction to form SFCA. Given that $C_2(F_{1-x}A_x)$ was not directly involved in the reaction to form SFCA-I, and CF and Fe_2O_3 do not incorporate significant amounts of Al^{3+},[25] it is considered likely that CFA did react to provide the Al^{3+} content required to form SFCA-I. **Figure 9** shows a backscattered electron micrograph of the

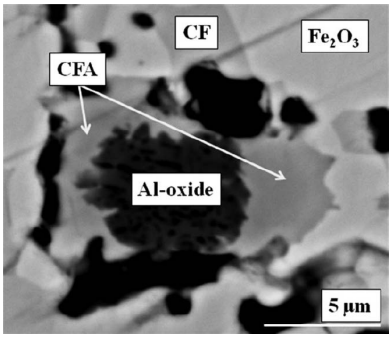

Fig. 9. Backscattered electron micrograph of the product of the heat/quench experiment performed at 1 323 K for 24 h at pO_2 = 0.21 atm, showing CFA, Fe_2O_3, CF and unreacted Al-oxide. The black areas are pores.

product of the heat/quench experiment performed at pO_2 = 0.21 atm and 1 323 K for 24 h, with unreacted amorphous Al-oxide encased by CFA, meaning that CFA reacts before the Al-oxide itself is available. EDS analysis confirmed that CF contained a very low concentration of Al^{3+} similar to that which was determined by Webster *et al*.[25] Eqs. (10) and (11) summarise the reactions involved in the formation of SFCA-I and SFCA at pO_2 = 0.21 atm:

$$Fe_2O_3 + CF + SiO_2 + CFA + \text{Al-oxide} \rightarrow \text{SFCA-I} \quad \ldots\ldots (10)$$

$$Fe_2O_3 + CF + SiO_2 + \text{Al-oxide} \pm \text{SFCA-I} \rightarrow \text{SFCA} \quad \ldots\ldots (11)$$

4. Conclusion

The formation mechanisms of SFCA and SFCA-I iron ore sinter phases during heating of a synthetic iron ore sinter mixture in the range 298–1 623 K and at pO_2 = 0.21, 5×10^{-3} and 1×10^{-4} atm were determined using *in situ* XRD. Oxygen partial pressure has a significant effect on the formation of SFCA-I and SFCA. Importantly, if the oxygen partial pressure is too low, then desirable SFCA-I will not form. Rather, a Ca-rich ferrite phase designated CF_{AlSi}, will form through reaction between $C_2(F_{1-x}A_x)$, CF, SiO_2 and Fe_3O_4. On the other hand, if the pO_2 is too high, the thermal stability range of SFCA-I before the formation of SFCA will be reduced. In addition, CFA, which had previously been determined to be a key precursor phase in the formation of SFCA at pO_2 = 5×10^{-3} atm, was also observed to form at pO_2 = 0.21 and 1×10^{-4} atm with the amount decreasing with increasing pO_2. Future work will investigate the effect of pO_2 on the equilibrium phase assemblages produced from a number of different starting mixtures at a number of temperatures in the range 1 423–1 573 K. It will also implement *in situ* XRD to investigate the phase formation mechanisms, during heating in the range 298–1 623 K, in sinter mixtures with compositions designed to form SFCA-I instead of SFCA, and will be the first *in situ* XRD-based study to do so.

Acknowledgements

ANSTO are acknowledged for providing financial support for this research. This research was performed, in part, on the powder diffraction beamline (10BM1) at the Australian Synchrotron, Victoria, Australia, under beamtime award AS113/PD4160. The authors wish to thank: Caroline Johnson (CSIRO Process Science and Engineering) for assistance with synchrotron data collection; Matthew Glenn (CPSE) for assistance with scanning electron microscopy; Nick Wilson (CPSE) for assistance with EPMA analyses; and Lisa Famularo (CPSE) for conducting Fe^{2+} determination.

REFERENCES

1) P. R. Dawson, J. Ostwald and K. M. Hayes: *T. I. Min. Metall. C*, **94** (1985), 71.
2) T. R. C. Patrick and R. R. Lovel: *ISIJ Int.*, **41** (2001), 128.
3) L-H. Hsieh and J. A. Whiteman: *ISIJ Int.*, **29** (1989), 24.
4) L-H. Hsieh and J. A. Whiteman: *ISIJ Int.*, **29** (1989), 625.
5) T. Mukherjee and J. A. Whiteman: *Ironmaking Steelmaking*, **12** (1985), 151.
6) J. Ostwald: *BHP Technical Bulletin*, **25** (1981), 13.
7) N. J. Bristow and A. G. Waters: *T. I. Min. Metall. C*, **100** (1991), 1.
8) I. Shigaki, M. Sawada and N. Gennai: *Trans. Iron Steel Inst. Jpn.*, **26** (1986), 503.
9) C. E. Loo, K. T. Wan and V. R. Howes: *Ironmaking Steelmaking*, **15** (1988), 279.
10) W. G. Mumme, J. M. F. Clout and R. W. Gable: *Neues Jahrb. Miner. Abh.*, **173** (1998), 93.
11) J. Hancart, V. Leroy and A. Bragard: *C. N. R. M. Report*, DS 24/67 (1967), 3.
12) S. N. Ashan, T. Mukkerjee and J. A. Whiteman: *Ironmaking Steelmaking*, **10** (2003), 54.
13) T. R. C. Patrick and M. I. Pownceby: *Metall. Mater. Trans. B*, **32** (2001), 1.
14) W. G. Mumme: *Neues Jahrb. Miner. Abh.*, **178** (2003), 307.
15) T. van den Berg and J. P. R. de Villiers: 9th Int. Cong. for Applied Mineralogy, Brisbane, QLD, (2008), 713.
16) T. van den Berg and J. P. R. de Villiers: *T. I. Min. Metall. C*, **118** (2009), 214.
17) J. McAndrew and J. M. F. Clout: Proc. of the 4th China-Australia Symp. on the Technology of Feed Preparation for Ironmaking, Dampier, Australia, (1993), 1.
18) Y. Hida, M. Sasaki, K. Sato, M. Kagawa, M. Takeshi, H. Soma, H. Naito and M. Taniguchi: *Nippon Steel Tech. l Rep.*, **35** (1987a), 59.
19) M. Sasaki and Y. Hida: *Tetsu-to-Hagané*, **68** (1982), 563.
20) Y. Hida, J. Okazaki, K. Ituh and M. Sasaki: *Tetsu-to-Hagané*, **73** (1987b), 1893.
21) F. Matsuno: *Trans. Iron Steel Inst. Jpn.*, **19** (1979), 595.
22) F. Matsuno and T. Harada: *Trans. Iron Steel Inst. Jpn.*, **21** (1981), 318.
23) N. V. Y. Scarlett, M. I. Pownceby, I. C. Madsen and A. Christensen: *Metall. Mater. Trans. B*, **35** (2004), 929.
24) N. V. Y. Scarlett, I. C. Madsen, M. I. Pownceby and A. N. Christensen: *J. Appl. Crystallogr.*, **37** (2004), 362.
25) N. A. S. Webster, M. I. Pownceby, I. C. Madsen and J. A. Kimpton: *Metall. Mater. Trans. B*, **43** (2012), 1344.
26) Bruker, TOPAS Version 4.2, Bruker AXS Inc., Madison, Wisconsin, USA, (2009).
27) R. Blake, R. Hessevick, T. Zoltai and L. Finger: *Am. Mineral.*, **51** (1966), 123.
28) E. N. Maslen, V. A. Strel'tsov, N. R. Strel'tsova and N. Ishizawa: *Acta Crystallogr.*, **B51** (1995), 929.
29) H. Saalfeld and M. Wedde: *Z. Krystallogr. Krist.*, **139** (1974), 129.
30) G. A. Lager, J. D. Jorgensen and F. J. Rotella: *J. Appl. Phys.*, **53** (1982), 6751.
31) I. Oftedal: *Z. Phys. Chem.*, **128** (1927), 135.
32) P. Berastegui, S.-G. Eriksson and S. Hull: *Mater. Res. Bull.*, **34** (1999), 303.
33) D. F. Decker and J. S. Kasper: *Acta Crystallogr.*, **10** (1957), 332.
34) W. C. Hamilton: *Phys. Rev.*, **110** (1958), 1050.
35) K. Wallwork, B. Kennedy and D. Wang: *AIP Conf. Proc.*, **879** (2007), 879.
36) G. S. Pawley: *J. Appl. Crystallogr.*, **14** (1981), 357.
37) K. Kihara: *Eur. J. Mineral.*, **2** (1990), 63.
38) J. S. Huebner: Research Techniques for High Temperature and High Pressure, ed. by G. C. Ulmer, Springer-Verlag, New York, (1971), 123.
39) M. I. Pownceby and J. M. F. Clout: *T. I. Min. Metall. C*, **109** (2000), 36.
40) N. V. Y. Scarlett and I. C. Madsen: *Powder Diff.*, **21** (2006), 278.
41) I. C. Madsen and N. V. Y. Scarlett: Powder Diffraction: Theory and Practice, ed. by R. E. Dinnebier and S. J. L. Billinge, The Royal Society of Chemistry, Cambridge, (2008), 298.
42) N. A. S. Webster, I. C. Madsen, M. J. Loan, R. B. Knott, F. Naim, K. S. Wallwork and J. A. Kimpton: *J. Appl. Crystallogr.*, **43** (2010), 466.
43) N. A. S. Webster, M. J. Loan, I. C. Madsen, R. B. Knott, G. M. Brodie and J. A. Kimpton: *J. Cryst. Growth*, **340** (2012), 112.